OPEN ACCESS

University of BRISTOL

Hansen, C. S., Marchetti, B., Karsili, T. N. V., & Ashfold, M. N. R. (2021). Ultraviolet Photodissociation of Gas-Phase Transition Metal Complexes: Dicarbonylcyclopentadienyliodoiron(II). *Molecular Physics*, *119*, [e1813343]. https://doi.org/10.1080/00268976.2020.1813343

Peer reviewed version

Link to published version (if available):
10.1080/00268976.2020.1813343

Link to publication record in Explore Bristol Research
PDF-document

This is the author accepted manuscript (AAM). The final published version (version of record) is available online via Taylor & Francis at https://doi.org/10.1080/00268976.2020.1813343 . Please refer to any applicable terms of use of the publisher.

University of Bristol - Explore Bristol Research
General rights

This document is made available in accordance with publisher policies. Please cite only the published version using the reference above. Full terms of use are available:
http://www.bristol.ac.uk/red/research-policy/pure/user-guides/ebr-terms/

Ultraviolet Photodissociation of Gas-Phase Transition Metal Complexes: Dicarbonylcyclopentadienyliodoiron(II)

Christopher S. Hansen,[1]* Barbara Marchetti,[2]* Tolga N.V. Karsili [2]* and Michael N.R. Ashfold [3]*

[1] School of Chemistry, University of New South Wales, Sydney NSW 2052, Australia

[2] University of Louisiana at Lafayette, Lafayette, Louisiana 70504, United States

[3] School of Chemistry, University of Bristol, Bristol BS8 1TS, United Kingdom

*For correspondence: christopher.hansen@unsw.edu.au, barbara.marchetti@louisiana.edu, tolga.karsili@louisiana.edu, mike.ashfold@bristol.ac.uk.

ABSTRACT

The ultraviolet photodissociation of the prototypical organometallic half-sandwich compound dicarbonylcyclopentadienyliodoiron(II) [η^5-CpFe(CO)$_2$I] has been studied in the gas phase across the wavelength range $260 \leq \lambda \leq 310$ nm using multi-mass velocity-map ion imaging with photoproducts detected using both resonance enhanced multiphoton and vacuum ultraviolet ($\lambda = 118.2$ nm) single photon ionization methods. Ion images recorded for the atomic iodine and the cyclopentadienyl photoproducts reveal fast, anisotropic components to their recoil velocity distributions. The experimental work is supported by multi-reference (spin-orbit averaged) electronic structure calculations that suffice to illustrate the high electronic state density in such transition metal complexes and provide insights into the rival fragmentation dynamics. The ground state parent molecule has singlet spin multiplicity, but the product energy disposal measured following Fe–Cp bond fission shows the involvement of nominally spin-forbidden transitions. The Fe–I and Fe–Cp bond fissions should both be viewed as homolytic and occurring on excited state potentials that are dissociative in the relevant ligand elimination coordinate.

1. INTRODUCTION

Transition metal containing compounds, and their interactions with light, find many roles in contemporary science [1] – with applications ranging from functional materials, such as photovoltaic devices,[2] to medicine (*e.g.* photodynamic therapy).[3,4] Catalysis is needed to promote the chemistry of hydrocarbons, given that they contain only strong and (relatively) unreactive C–H and C–C bonds. Catalytic chemistry involving hydrocarbons relies on the transient formation of weak σ-alkane complexes through a CH–metal interaction referred to as an 'agostic' bond.[5] Recent studies have demonstrated that such complexes, which are typically unstable in solution, can be prepared and even isolated following the photolytic cleavage of a metal–ligand (M–L) bond in an organometallic half sandwich compound,[6] *i.e.* a transition metal complex in which the M–L center is bound to a cyclic polyhapto ligand. Whilst photocatalysis is a well-known phenomenon, *e.g.* it is the principal process in dye-sensitized solar cells, this example highlights the on-going need for a better understanding of the (photo)fragmentation of such transition metal complexes.

The photochemistry of metal-containing compounds has long been of interest from a fundamental perspective, as a route to synthesizing other organometallic complexes as well as in photocatalysis applications.[7,8] Much recent mechanistic progress has stemmed from solution phase studies using, for example, time resolved infrared (TRIR) spectroscopy to distinguish and monitor the time evolution of spectral features associated with the precursor molecule, reaction intermediates and the eventual products.[9] TRIR studies of benzene chromium(0) tricarbonyl (η^6-BzCr(CO)$_3$), for example, allowed determination of the lifetime of the metal-to-carbonyl charge transfer excited state populated by photoexcitation at a wavelength $\lambda = 400$ nm and revealed adduct formation as a result of ligand exchange with the solvent (cyclohexane).[10] Ground state processes have been studied extensively in this way, with interpretation often guided by accompanying electronic structure calculations,[11] but unravelling excited state reactivity remains a challenge given the density of excited electronic states. As in many other areas of chemistry, reducing the complexity offers one route to developing understanding which, in the case of the photochemistry of metal-containing compounds, has encouraged investigations under isolated molecule (*i.e.* gas phase) conditions.

Early photofragment translational spectroscopy (PTS) experiments showed that the recoil velocity distributions of the M(CO)$_5$ fragments formed by $\lambda = 300$ nm excitation of M$_2$(CO)$_{10}$ (M = Re, Mn) were highly anisotropic.[12] The observed angular anisotropy implied prompt dissociation following an electronic excitation wherein the transition dipole moment (TDM) is

along the M–M bond, and was explained in terms of an M–M bond-centered $\sigma^* \leftarrow \sigma$ electron promotion. Later multiphoton ionization (MPI) time-of-flight (TOF) mass spectroscopy studies revealed M_2^+ (and M^+) fragment ions amongst the products formed by $\lambda = 337$ nm photolysis and subsequent MPI of these same decacarbonyls, however, implying that rival M–CO bond fission pathways operate also, even at this longer UV wavelength.[13]

Photolysis studies of gas phase $Mn_2(CO)_{10}$ at shorter excitation wavelengths (λ = 193 nm) revealed formation of electronically excited Mn* atoms.[14] Fe* atoms were similarly observed following λ = 248 nm photoexcitation of $Fe(CO)_5$ and rationalized in terms of a 'ladder-climbing' mechanism wherein photon absorption triggers the ejection of one (or more) ligands, leaving a metal-containing intermediate that can absorb one or more additional photons from the same (nanosecond (ns) duration) laser pulse and fragment further.[14] Other, wavelength-dependent photolysis studies of $Fe(CO)_5$ served to reinforce the conclusion that single photon absorption could trigger the loss of multiple CO ligands.[15] The validity of such mechanisms was further reinforced by two femtosecond (fs) pump–probe studies of $Fe(CO)_5$.[16,17] The first used λ = 400 nm pump and λ = 800 nm MPI probe lasers. (The ionized forms of) all $Fe(CO)_n$ ($n < 5$) intermediates were detected in TOF mass spectra measured at the shortest pump-probe time delays, but the ion yield spectra measured at longer time delays were interpreted by assuming that electronically excited parent molecules formed by absorption of two λ = 400 nm photons lose no fewer than four CO ligands within ~100 fs and that the surviving FeCO intermediate decays on a slightly longer (230 fs) timescale.[16] The second study involved one photon excitation at λ = 267 nm and a λ = 800 nm MPI probe, and reached somewhat different conclusions.[17] Again, all $Fe(CO)_n^+$ (n = 0-5) ions were detected, but the associated time constants were rationalized in terms of rapid loss of one CO ligand from the photoexcited parent molecule followed by the slower loss of a second CO from the internally excited $Fe(CO)_4$ photoproduct. The observed smaller fragment ions were ascribed to dissociative ionization of $Fe(CO)_n$ (n = 4, 5) species formed by the λ = 267 nm excitation. A recent reinvestigation of the λ = 266 nm photolysis of $Fe(CO)_5$ using X-ray photoelectron spectroscopy confirms the loss of successive CO ligands yielding, first, $Fe(CO)_4$ and then, on a longer timescale, $Fe(CO)_3$ fragments, and suggested that these processes occur solely on singlet potential energy surfaces (PESs) [18] – the feasibility of which has since been validated by coupled cluster response theory calculations.[19]

Gerber and co-workers also reported ultrafast pump-probe fragmentation studies of the half-sandwich metal complex of current interest, dicarbonylcyclopentadienyliodoiron(II) (η^5-

$CpFe(CO)_2I$, henceforth $CpFe(CO)_2I$), using λ = 400 nm pump pulses and detecting with a λ = 800 nm MPI probe pulse.[20] The time evolving parent and fragment ion yields were interpreted by assuming primary Fe–CO and Fe–I bond fission processes, with sequential loss of the remaining ligands leading to eventual detection of Fe^+ fragment ions. Again, the authors recognized possible ambiguities in distinguishing whether a given fragment ion was formed by MPI of the corresponding neutral fragment, by dissociative MPI of a larger neutral fragment, or by photodissociation of larger cations.[20] For completeness, we note that photoinduced Fe–I bond fission in $CpFe(CO)_2I$ has also been reported in solution, following continuous excitation at several different visible wavelengths in the range $488 \leq \lambda \leq 647$ nm.[21]

Here we report studies of the fragmentation dynamics following ns laser photoexcitation of $CpFe(CO)_2I$ in the gas phase at several UV wavelengths in the range $260 \leq \lambda \leq 310$ nm using a multi-mass velocity map imaging (VMI) spectrometer equipped with both resonance enhanced MPI (REMPI) and vacuum UV (VUV, λ = 118.2 nm) single photon ionization (SPI) detection capabilities. These studies yield new data regarding the recoil velocities (speed and angular distributions) of the I atoms in both the ground ($^2P_{3/2}$) and spin-orbit excited ($^2P_{1/2}$) (henceforth denoted as I and I*) states, and of the Cp fragments. Interpretation of these data is guided by density functional theory (DFT) calculations of the energies of the ground (S_0) state parent molecule and various possible fragment species, and by cuts through the S_0 state and the first few singlet and triplet excited state PESs along two of the bond stretch coordinates of interest ($R_{Fe–I}$ or $R_{Fe–CO}$), calculated at the complete active space self-consistent field (CASSCF) level of theory.

The ionization potential of CO (14.01 eV) is well above the energy provided by a single λ = 118.2 nm photon. Thus the present experiments cannot report directly on the formation of CO products. The presence of the metal atom means that CpFe(CO)I, the co-product of CO loss, should be amenable to ionization at λ = 118.2 nm. No significant signals corresponding to such large fragment ions were detected, but this is likely just a reflection of the efficiency of their dissociative ionization when excited at 118.2 nm. The present experiments do unequivocally demonstrate photoinduced loss of the I and Cp ligands, however, and confirm the previously reported [17] dominance of Fe^+ among the ions formed when exciting gas phase $CpFe(CO)_2I$ molecules with ns duration UV light pulses. This combined experimental and theoretical study provides new insights into the photodissociation of M–L bonds in the gas-phase. It also considers briefly the extents to which photochemical insights derived from gas phase studies

of a heavy- (*e.g*. I-) atom containing metal complex might extrapolate to other metal complexes and/or to the UV photoinduced chemistry of metal complexes in the condensed phase.

2 METHODS

2.1 Experimental

The experimental data were acquired using a VMI apparatus and the resulting images processed as detailed elsewhere.[22,23] $CpFe(CO)_2I$ (Sigma Aldrich, 99% stated purity) was packed in a stainless steel in-line filter positioned before a pulsed nozzle, heated to ~50 °C, entrained in helium carrier gas (~600 mbar) and skimmed prior to entering the differentially pumped photolysis chamber along the principal axis of the ion optics assembly. The early time part of the molecular beam was intersected between the repeller and extractor electrodes by one or more ns laser pulses. For the two-color experiments, the UV photolysis and the λ = 118.2 nm SPI probe laser outputs were counter-propagated along an axis orthogonal to the principal axis of the spectrometer, with a pump-probe delay time of 25 ns, while a single (frequency doubled) tunable dye laser served as the source of both the photolysis and probe radiation for the experiments involving 2+1 REMPI detection of I and I* fragments. All data in the present study were recorded under a consistent set of electrode voltages, which were calibrated for ion velocity by monitoring the total iodine atom (I_{tot}), the I and/or the I* signals from the UV photolysis of CH_3I at various times during the data collection period. Ion event lists were recorded using the fast-framing PImMS2 camera [24] from which images of any selected ion (with mass to charge ratio m/z) were obtained by selecting just the central 25 ns time slice of the relevant signal in the ion time-of-flight (TOF) spectrum. These slice images (which typically constitute ~10-15% of the whole TOF distribution of the ion of interest) were analyzed without further reconstruction or processing other than, in the case of the Cp fragment images, an attempt at background correction by subtracting the corresponding image acquired for an equivalent number of experimental cycles with only the λ = 118 nm proble laser light present.

2.2 Theoretical

The parent ground (S_0) state minimum was optimized using DFT with the Coulomb Attenuating Model-B3LYP (CAM-B3LYP) functional [25] within Gaussian09,[26] with the relativistic effective core potential LANL2DZ basis set [27] accounting for 46 frozen core electrons for the iodine atom and 10 for iron. Computation of the ground state harmonic frequencies followed, at the

same level of theory. The same methods were used to optimize many of the possible radical structures that result following loss of different ligands.

Selected cuts through the spin-orbit averaged (SOA) 'unrelaxed' (*i.e.* rigid-body) PESs (PECs) for the parent S_0 state and the lower lying excited states were computed by scanning, respectively, the Fe–I or Fe–CO bond stretch coordinates (*i.e.* $R_{Fe–I}$ or $R_{Fe–CO}$) using CASSCF theory coupled to the DEF2-SVP basis set with a 28 core-electron effective core potential on the I atom. In both cases, the scan was from large internuclear separation to progressively shorter values of R, with all other atoms held at their ground state equilibrium positions. For the $R_{Fe–I}$ coordinate, the scan maintained C_S symmetry and employed an active space of 12 electrons in 10 orbitals (the three highest occupied and two lowest unoccupied orbitals of both A' and A" symmetry, depicted in Figure S1 in the Supplementary Information (SI)). For the $R_{Fe–CO}$ stretch coordinate, the molecule breaks C_S symmetry upon bond extension, and one (the CO) or both of the resulting fragments has a closed-shell electronic configuration. As such, the active space used for the $R_{Fe–CO}$ calculations presented challenges and, after careful testing, an active space of 12 electrons in 9 orbitals (the 6 highest occupied valence orbitals and the 3 lowest unoccupied orbitals) was deemed appropriate to describe the associated chemistry. The CASSCF calculations were performed using the Molpro 2015 computation package.[28] The returned energies and transition dipole moments were used to calculate the oscillator strengths, as previously.[29] Calculating PECs as a function of distance between Fe and the centre of the Cp ring proved even more challenging, as the minimum energy path on the S_0 PES involves a progressive ring-slip rather than fragmentation, and was not pursued further.

3 RESULTS and DISCUSSION

3.1 Electronic spectrum of $CpFe(CO)_2I$

Ground state $CpFe(CO)_2I$ molecules adopt the classic 'piano stool' structure shown in Figure 1, with a mirror plane intersecting one of the carbon atoms of the Cp ring, the Fe and I atoms. The electronic absorption spectrum of $CpFe(CO)_2I$ (in cyclohexane solution, Figure 1) shows absorption maxima at ~215 nm, ~270 nm and ~355 nm, and agrees well with previous reports of (just the longer wavelength part of) this spectrum in other organic solvents.[21]

A qualitative understanding of this electronic spectrum can be gained from the traditional molecular orbital (MO) diagram shown in Figure 2. The tetrahedral geometry leads to a low-spin configuration of the Fe-centered *d*-orbitals, which can be understood by group-symmetry

arguments and by picturing the ways in which the electrons of the ligands interact with the *d*-orbitals of the Fe. Within this configuration, the d_z^2 and $d_{x^2-y^2}$ orbitals lie at lower energies than the d_{xy}, d_{yz} and d_{xz} orbitals. Figure 2 was constructed by assembling the molecule from an Fe^{2+} cation, Cp^- and I^- anions and two neutral CO ligands. First, we consider interactions between the Fe^{2+} ion and the electrons centred on Cp^-. Cp^- has six π-electrons distributed in five p_x-orbitals arranged as three bonding π and two antibonding π^* orbitals. These π and π^* orbitals (which, as Figure 2 shows, transform as a' (×3) and a'' (×2) in C_S) interact with the *d*-orbitals of the metal to yield five occupied $d\pi$ and five virtual $d\pi^*$ MOs. Three of these bonding orbitals are filled by the Cp^- ligand donating six electrons. In similar vein, the CO ligands each possess an occupied *p* orbital; together, these transform as a symmetric (a') and antisymmetric (a'') ligand type orbital (LTO) pair. Each LTO overlaps with a Fe *d*-orbital of the appropriate symmetry to yield pairs of σ_{Fe-CO} and σ_{Fe-CO}^* MOs that are filled, datively, by donation of two electrons from each CO ligand. Lastly, I^- presents a triad of 5*p*-valence orbitals. One of these is correctly oriented to bond with Fe^{2+}, to give σ and σ^* MOs localized around the Fe–I bond. The other *p* orbitals are non-bonding (*n*) orbitals and transform as the highest occupied MOs (HOMOs).

The dominant orbital promotions associated with transitions from the ground state of $CpFe(CO)_2I$ to the first few (nominally) singlet and triplet excited states of A' and A" symmetry are listed in Table S1. Given the presence of the heavy Fe and I atoms, the excited state energies returned by, for example, the 'unrelaxed' scans from large R_{Fe-I} to the ground state equilibrium geometry (see Section 3.6) should be viewed as illustrative only. Nonetheless, the calculations serve to illustrate several key features and shape the interpretation of the experimental data. As Figure S1 shows, the occupied MOs are generally diffuse and delocalized over much of the molecule. The excited state density is high (17 singlet and triplet excited states are predicted with excitation energies <5 eV). Many of the excitations display significant ligand → metal charge transfer (LMCT) character and the transitions with greatest predicted oscillator strength both involve $\pi^* \leftarrow n/\pi$ promotions and lie in the UV spectral region. The weaker absorption at longer wavelengths is plausibly associated with transitions to (nominal) triplet excited states.

3.2 Ion TOF mass spectra

Figure 3 shows the ion mass spectrum obtained by λ = 118.2 nm SPI following excitation of a jet-cooled sample of $CpFe(CO)_2I$ at λ = 275 nm, along with the corresponding one-color spectra obtained by blocking the photolysis or the photoionization laser beam. The *m*/*z* scale in Figure

3 is determined from the TOFs of ions measured assuming that the photoionization event defines time zero. Ions of any given *m*/*z* formed solely by the photolysis laser pulse will have been created ~25 ns earlier, and careful inspection of the figure reveals such ions appearing at appropriately shifted (lower) *m*/*z* values. The peak at *m*/*z* 56 (attributable to Fe^+ ions) dominates all three spectra, and the experimental resolution is sufficient to reveal a shoulder attributable to $^{54}Fe^+$ (5.8% natural abundance). The two-color spectrum shows additional peaks that are most logically attributed to, in order of decreasing *m*/*z* value, $CpFe(CO)_2I^+$, $CpFe(CO)I^+$, $CpFeI^+$, CpI^+, FeI^+, I^+, $FeCp^+$ and Cp^+ and further features at *m*/*z* 254 (I_2^+ impurity) and *m*/*z* 91 and 63 (which we tentatively assign to FeI^{2+} and I^{2+}, respectively). The relative intensities of these features are sensitive to the pump and probe laser intensities and in several cases are almost entirely λ = 118.2 nm laser induced. Without knowledge of the respective photoionization cross-sections, the propensities for dissociative ionization of the parent molecule, *etc.*, it is not possible to relate the various *m*/*z* peak intensities to the relative yields of neutral photofragments formed by UV photolysis. However, the data in Figure 3 indicate two-color contributions to the CpI^+, FeI^+, $FeCp^+$ and, particularly, the I^+, Cp^+ and Fe^+ ion yields. Analysis of the respective ion images provide further insights into the various ion formation mechanisms.

3.3 Photofragment Ion Images

The present study is blind to CO photofragments but returns images of the abundant ions appearing in Figure 3. A representative Fe^+ ion image and the unsmoothed kinetic energy (KE) distribution derived from its analysis are shown in the SI (Figure S2). The image is isotropic, shows maximum intensity at its center and no discernible fine structure under any combination of pump and probe laser intensities investigated. Such a KE distribution is typically viewed as a signature of fragments arising via the dissociation of highly internally excited species and, in the present context, is most readily attributed to dissociative ionization of the parent molecule and/or the more abundant Fe-containing photofragments. The images recorded for the other, less intense, Fe containing fragment ions are similar to that of the Fe^+ ions shown in Figure S2. The identification of *m*/*z* peaks attributable to species like CpI^+, that require isomerization prior to fragmentation, provide further evidence for the transitory formation of larger cationic species with high levels of internal excitation.

The I^+ and Cp^+ fragment images, in contrast, all reveal formation of translationally excited products. The left hand column in Figure 4 shows representative images recorded following photolysis at λ ~266 nm of (a) the total I atom (I_{tot}) yield and (d) the Cp fragments detected by

SPI and of (b) the I and (c) the I* atoms detected by (2+1) REMPI. These images, as with all those displayed in the paper, have been symmetrized prior to display. Each shows an anisotropic annular feature, which we fit to the standard expression

$$T(\theta) \propto 1 + \beta P_2(\cos\theta) \qquad (1)$$

for describing the angular distribution of fragments arising in a one photon dissociation process.[30] $P_2(\cos\theta)$ in eq. (1) is the second Legendre polynomial, θ is the angle between the fragment recoil velocity, v, and the polarization vector $\boldsymbol{\varepsilon}$ of the radiation inducing the bond fission (shown by the double headed arrow in the top right of Figure 4(a)), and β is the recoil anisotropy parameter. β takes limiting values of –1 and +2, in the cases that a fragment recoils axially following excitation via a transition for which the TDM is aligned, respectively, perpendicular and parallel to the breaking bond. $\beta = 0$ describes an isotropic recoil velocity distribution. The right hand column of Figure 4 displays the velocity distributions derived from the corresponding images, overlayed (red circles) with the best-fit β parameter for each velocity data point within the specified range. The best-fit values of β derived from the I_{tot} and I* images shown in Figures 4(a) and 4(c) both increase with increasing v, from near zero to ~ +1.4 at the leading edge of the distributions, while the β derived from the I image (Figure 4(b)) increases to a maximum of ~ +1. All then decline towards zero at the very highest velocities detected.

The Cp images contain both a fast, anisotropic component, again characterized by $\beta \sim +1$ at the KE of maximum intensity, and an intense isotropic central feature. The central feature is deliberately saturated in the image shown in Figure 4(d) in order to clarify the fast, anisotropic component. Some of the central feature is one-color in origin, but its total intensity in two-color images such as that shown in Figure 4(d) is consistently greater than just the sum of the two one-color components; part of the central feature in the Cp images is deduced to be two-color signal.

Attention is now focussed on the anisotropic annular components in these images. Figure 5(a) shows unsmoothed KE distributions derived from SPI-detected I_{tot} images recorded at ten wavelengths in the range $260 \leq \lambda \leq 310$ nm. Similar plots derived from one-color REMPI-detected I and I* images recorded at three closely matched pairs of wavelengths are shown in Figures 6(a) and 6(b), where they are also compared with the I_{tot} distribution recorded at the closest equivalent photolysis wavelength (Figure 6(c)). The abscissae in these figures are the KEs of the imaged iodine fragments, KE_I, rather than a total kinetic energy release (TKER), since the latter quantity requires knowledge of the partner fragment mass (m_R) – and thus the

fragmentation process – which we discuss in the next section. As Figure 6(a) shows, the KE distribution derived from the I atom image recorded at λ = 304 nm matches well with that derived from the 118.2 nm SPI-detected I_{tot} image from photolysis at λ = 303.6 nm. This is logical, given the ~20-times larger ionization cross-section of I (*cf.* I*) atoms at λ = 118.2 nm.[31] The apparently poorer agreement between the REMPI-detected I atom and λ = 118.2 nm SPI-detected I_{tot} distributions found at the shorter photolysis wavelengths is considered later. The shoulder in Figure 6(c) labelled 'CH_3I' arises from I atoms from the photodissociation of methyl iodide that was used periodically to calibrate the experiment.

The KE distributions derived from the λ = 118.2 nm SPI-detected Cp images recorded at the same ten photolysis wavelengths are shown in Figure 7(a). Again, the major part of these distributions peaks away from zero KE, consistent with dissociation on a PES that is, at some point at least, repulsive in the coordinate of interest.

3.4 I and I* fragment formation

The very different λ = 118.2 nm SPI efficiencies of I and I* fragments [31] suggests that the I_{tot} distributions shown in Figure 4 are likely to be dominated by the I fraction within the total I + I* dissociation yield. All the I_{tot} KE distributions appear unimodal. The fastest ~70% of each distribution has been fitted to a Gaussian function to determine the most probable KE, KE_{mp}, with an uncertainty corresponding to the Gaussian root-mean-square (RMS) width of the fitted function. As shown in Figure 5(b), KE_{mp} scales linearly with the photolysis photon energy, E_{phot}. Extrapolating the uncertainty-weighted linear fit to the KE_{mp} *vs* E_{phot} plot to KE_{mp} = 0 returns an intercept of 10600 ± 3100 cm^{-1} (1.31 ± 0.38 eV, where the quoted uncertainty represents the 95% confidence limit). This value is consistent with Fe–I bond fission following photoexcitation of the jet-cooled $CpFe(CO)_2I$ parent. Such an attribution is logical given that $CpFe(CO)_2I$ is the most abundant I-containing species present, and the only species likely to be present in the limited set of internal quantum states and with the narrow spread of velocities required to yield photofragment ion images with the measured clarity and resolution. This Fe–I bond dissociation energy matches well with literature recommendations (1.28 eV [32]) and with the results of the DFT calculations of the (SOA) ground state energies of the parent molecule and the various sets of asymptotic dissociation products listed in Table S2 in the SI.

The ground state $CpFe(CO)_2$ fragment has doublet spin multiplicity (Table S2) and, as Table 1 shows, the (SOA) $^2CpFe(CO)_2$ + I dissociation limit is calculated to lie 1.71 eV above the parent ground state minimum. To compare this with the experimentally derived value, we

subtract $A_I/3$, where A_I is the spin-orbit splitting in the iodine atom (7603 cm^{-1} or 0.943 eV),[33] yielding $D_{e(calc)}(CpFe(CO)_2–I)$ = 1.40 eV – in good accord with the experimental determination. Strictly, this comparison also requires a further correction for zero-point energy (ZPE) effects, but the ZPE associated with the three vibrational modes lost on Fe–I bond fission will be much smaller than the experimental uncertainty and is thus neglected. This analysis implies that photoexcitation of the singlet ground state parent molecule yields two products with doublet spin multiplicity, which can be accommodated by dissociation on excited state PESs with either singlet or triplet spin multiplicity.

Given that the I_{tot} signal is dominated by ground state I atoms from one photon photolysis of parent $CpFe(CO)_2I$ molecules, conservation of linear momentum requires that

$$\mathrm{TKER} = \mathrm{KE_I}[1 + (m_\mathrm{I}/m_\mathrm{R})] \qquad (2)$$

where m_I and KE_I are, respectively, the mass and the experimentally derived KE of the I atom fragment and $m_\mathbf{R}$ = 176.97 u is the mass of the $CpFe(CO)_2$ partner. Thus the appropriate TKER scale for each of the distributions in Figure 5 is simply $1.717 \times KE_I$. Persisting with the literature recommendation $D_0(CpFe(CO)_2–I)$ = 1.28 eV, the derived $TKER_{mp}$ values imply that the fraction of the available energy (*i.e.* $E_{avl} = E_{phot} - D_0(CpFe(CO)_2–I)$) partitioned into translation of the $CpFe(CO)_2$ + I products, f_{TKER}, is ~0.33 at all wavelengths studied, leaving about two thirds of E_{avl} in other degrees of freedom ($f_{non\text{-}TKER}$ ~0.67). A similar analysis of the energy disposal accompanying I* product formation returns f_{TKER} ~0.45 and $f_{non\text{-}TKER}$ ~0.55. These non-TKER fractions equate to ~1.9 eV or ~2.3 eV for the $CpFe(CO)_2$ products formed with ground state I atoms at, respectively, λ = 310 and 260 nm, or ~1.3 eV for the $CpFe(CO)_2$ products formed with I* atoms at λ = 266.6 nm. The fact that $f_{non\text{-}TKER}$ for a given product pair is a near-constant fraction of E_{avl}, rather than a constant energy, tends to rule out specific electronic excitation of the $CpFe(CO)_2$ product as a likely sink for the 'missing' energy. Rather, we conclude that the geometry changes accompanying parent electronic excitation and subsequent Fe–I bond fission result in substantial internal (vibrational) excitation of the $CpFe(CO)_2$ co-fragment. Given the energetics reported in Table 1, this conclusion suggests that some of the most internally excited $CpFe(CO)_2$ products formed at the shorter excitation wavelengths could undergo secondary unimolecular decay, releasing a CO product (with low kinetic energy).

We now return to consider the differences between the REMPI-detected I atom and the SPI-detected I_{tot} distributions measured at the shorter photolysis wavelengths (Figure 6). The

REMPI-detected I atom image shows signal extending to higher KE_I values that is much less evident in the I_{tot} data. Given the relative laser intensities in the two experiments, molecules in the interaction region must be more susceptible to multiphoton excitation in the case of the REMPI study. Thus the most translationally excited I atoms in these velocity distributions, which show reduced recoil anisotropy ($\beta < 1$, Figure 4) and are more evident in the REMPI detected images (Figures 6(b) and 6(c)), are most likely attributable to a two (UV) photon dissociation process involving, either, excitation to super-excited states of the parent lying above its first ionization potential (7.77 eV),[34] or to photodissociation of internally excited I containing fragments formed by initial one photon induced Fe–CO or Fe–Cp bond fission.

3.5 Cp fragment formation

Figure 7 shows the KE distributions of the Cp fragments measured by SPI following photoexcitation at the same ten UV wavelengths. As with the I and I* fragments, these KE distributions peak away from zero. However, the Cp distributions also contain varying amounts of signal at KE_{Cp} ~0 which reflects the difficulty of subtracting the one-color contribution (mainly from the λ = 118.2 nm laser). From hereon we focus on the faster, two-color component. Again, the recoil anisotropy parameter increases across each distribution, reaching $\beta \sim +1$ at the leading edge, again implying that the ligand is lost on a timescale that is shorter than the parent rotational period (*i.e.* within, at most, a few ps). As with the I_{tot} data, the fastest ~70% of each distribution has been fitted to a Gaussian function to yield KE_{mp} values that increase with E_{phot}. Extrapolating a linear fit to the KE_{mp} *vs* E_{phot} plot (Figure 7(b)) to KE_{mp} = 0 returns an intercept of 19200 ± 4500 cm^{-1} (2.38 ± 0.56 eV). Given the laser intensities employed, the attributes of the images, and the fact that the measured KE_{Cp} values are all much less than E_{phot}, it is again logical to assign these products to one photon dissociation of the jet-cooled parent molecule. This returns an experimentally determined strength of the Fe–Cp η_5-linkage of 2.38 ± 0.56 eV, that matches well with that reported in Table 1 for dissociation to the respective ground state (*i.e.* $^4Fe(CO)_2I$ + ^2Cp) products. Given this bond strength, the derived $TKER_{mp}$ values (*i.e.* 1.272× the KE_{Cp} values from Figure 7) imply that the fractions of the available energy partitioned into translation and internal excitation of the $Fe(CO)_2I$ + Cp products are, respectively, f_{TKER} ~0.70 and $f_{non\text{-}TKER}$ ~0.30 at all wavelengths studied. This analysis implies eventual dissociation on an excited state PES with nominal triplet (or quintet) spin multiplicity and reiterates the conclusion that spin-orbit coupling effects are important in the excited state photophysics of this molecule.

3.6 Insights from theory

The orbital correlations (Figure 2) hint that most excitations should induce LMCT transitions, and the SOA-PECs along $R_{Fe–I}$ displayed in Figures 8(a) and 8(b) indicate that the net effect of many of the electron promotions is the development of $\sigma_{Fe–I}$* antibonding character and Fe–I bond fission. Approximate state assignments in the vertical region were listed in Table S1, but detailed discussion of these PECs is unwarranted given the approximate nature of the calculations.

The energetics (Table 1 and Figure 5) imply that UV photoexcitation of $CpFe(CO)_2I$ in the gas phase results in homolytic Fe–I bond fission. This conclusion contrasts with the heterolytic bond fission proposed in a previous solution phase, visible wavelength photolysis study of the molecule.[21] The present conclusion is reinforced by the calculated dissociation limit for forming the $CpFe(CO)_2^+ + I^-$ ion-pair products that would result from heterolytic bond fission, which is ~4 eV higher than the $^2CpFe(CO)_2 + {}^2I$ radical-pair limit. It is also unsurprising. A dissociative excited state PES necessarily involves a repulsive long-range interaction between the fragments, whereas a bound state PES will be attractive at long-range. In the present context, the latter is achieved if the electron in the singly occupied 5*p* orbital of the I atom forms a spin-pair with the odd-electron in one of the five *d*-orbitals of the Fe center; such an interaction correlates to the singlet ground state of $CpFe(CO)_2I$. But one can conceive of many situations where the $CpFe(CO)_2$ + I interaction must be repulsive at long range. For example, the dominant electronic configurations of several of the lower PECs at large $R_{Fe–I}$ in Figure 8 involve three Fe–I bond centred electrons (two in the $\sigma_{Fe–I}$ orbital and one in the $\sigma_{Fe–I}$* orbital).

The prior UV photoexcitation study of $CpFe(CO)_2I$ also suggests a non-zero quantum yield for the rival Fe–CO bond fission channel,[20] and Figure 2 illustrates the feasibility of populating excited states involving $\sigma_{Fe–CO}$* orbitals. CO is the quintessential two-electron donor ligand. Dissociation of the Fe–CO bond on the ground state PES must occur heterolytically: the electron pair is carried away by the CO, leaving an empty *d*-orbital on Fe and yielding closed-shell CpFe(CO)I + CO fragments. This is the only PES that can correlate to this particular combination of products.[35] Homolytic Fe–CO bond fission in this case would yield a (high energy) ion-pair. However, as Figures 9(a) and 9(b) show, theory predicts several low lying singlet and triplet excited states, with the first excited T_1 PEC correlating to the lowest energy $^3CpFe(CO)I$ + CO limit. The higher energy PECs in this figure all correlate to excited states of CpFe(CO)I along with a ground ($^1\Sigma$) state CO molecule and most are repulsive in the $R_{Fe–CO}$

coordinate. The closed shell character of the CO product ensures that each parent state correlates diabatically with a unique product asymptote.

As noted in section 2.2, all attempts at calculating PECs as a function of distance between Fe and the centre of the Cp ring on the S_0 PES returned a progressive ring-slip, rather than the dynamic (*i.e*. non-statistical) fragmentation process implied by the translationally excited Cp photoproducts revealed in the Cp^+ images (Figure 7). This observation might seem surprising, given the five $d\pi$ bonding orbitals associated with the η^5-Cp–Fe interaction. But these are relatively weak bonding interactions. The high density of electron-pairs confined within the small region around Fe–Cp causes greater electron-pair repulsion than in many more traditional bonding environments and we conclude that photoinduced electron promotion to one of the $d\pi^*$ orbitals is sufficient to induce Fe–Cp bond fission on a potential that is repulsive (at least at larger Fe–Cp separations). Again, the deduced energy disposal implies that the bond cleavage is homolytic, forming $Fe(CO)_2I$ + Cp radicals in their electronic ground states. This can be understood by recognizing that the infinitely separated Cp radical contains five electrons in three bonding π orbitals, two of which are degenerate (recall Figure 2). One of these degenerate orbitals contains an odd-electron, the other is doubly occupied. As in the case of Fe–I bond fission, an appropriate spin-paired interaction between the singly-occupied Cp orbital and a singly occupied *d*-orbital of the $Fe(CO)_2I$ radical correlates with the singlet ground state of $CpFe(CO)_2I$, but the alternative parallel spin encounter, and instances where a doubly occupied orbital of Cp approaches the singly occupied *d*-orbital of the $Fe(CO)_2I$ radical, will yield repulsive long-range interactions and correlate with excited state configurations at shorter $R_{Fe–Cp}$ separations.

3.7 Photofragmentation mechanism(s)

The present data demonstrate neutral I and Cp ligand loss following one photon excitation of $CpFe(CO)_2I$ at all wavelengths investigated in the range $260 \leq \lambda \leq 310$ nm. Both imaged ligands exhibit (non-limiting) parallel recoil anisotropies, the magnitudes of which increase with increasing v.

With regard to I atom loss, the UV photodissociation dynamics of $CpFe(CO)_2I$ shows parallels with that of RI (R = alkyl, aryl, *etc.*) molecules, wherein the eventual fragmentation is similarly driven by nuclear motions on excited state potentials arising as a result of electron promotion to an orbital centred on, in these cases, the C–I bond.[36-39] As with these RI molecules, any quantitative discussion of the photophysics of $CpFe(CO)_2I$ would clearly need to recognize the

substantial spin-orbit splitting of the I atom and the non-adiabatic couplings between PESs leading to the I and I* product limits. Qualitatively, however, the parallels are clear. The long wavelength UV absorption of iodobenzene (PhI), for example, is assigned to population of triplet excited states, and the lowest energy (SOA-)PESs correlating to Ph + I products are associated with triplet states with an electron in the σ_{C-I} * orbital.[38] In the present case, Fe–I bond fission is shown to yield ^{2}CpFe(CO)$_2$ + I products – which could arise via singlet and triplet excited state photochemistry. Further, the I atoms formed in the UV photolysis of PhI, of the variously fluorinated iodobenzenes [39] and of CpFe(CO)$_2$I all display positive recoil anisotropy parameters and have KE distributions that peak well above zero (consistent with bond fission on a repulsive PES) but also well below the maximum allowed by energy conservation (implying substantial internal excitation in the radical co-fragment).

Such observations can be accommodated by a model that recognizes the high density of accessible excited electronic states and assumes that excitation at any given wavelength populates several such states via TDMs that span a range of alignments relative to the breaking bond of interest. Some of these molecules could be promoted to excited states with dissociative character in the R_{Fe-I} (or R_{Fe-Cp}) coordinates and dissociate on timescales shorter than the rotational period, yielding the most anisotropic, translationally excited I (or Cp) fragments. Others may be promoted to states that are bound in the coordinates of interest and have to undergo more extensive intramolecular vibrational redistribution (IVR) and non-adiabatic coupling to the dissociation continua associated with release of the I or I* (or Cp) ligands. These rearrangements and couplings could result in a greater partitioning of E_{avl} into parent vibrational motion, much of which is likely to be in modes orthogonal to the dissociation coordinate and will thus tend to map into vibrational motion in the polyatomic fragments. The release of these products (relative to the parent rotational period) could occur on a longer timescale. Such factors would favor less translationally excited products with lower recoil anisotropy – consistent with observation.

Though the present experiments are blind to any CO photofragments, we note that the Fe–CO bond is calculated to be weaker than the Fe–I bond (Table 1) and that Fe–CO bond fission was proposed as the most facile decay channel in the previous ultrafast pump-probe studies of this molecule.[20] Analogy with the deduced energy disposals in the products from Fe–I and Fe–Cp bond fission in the present study, and with the prior λ = 267 nm photolysis studies of Fe(CO)$_5$ [17,18] encourages the view that any CpFe(CO)I fragments formed by Fe–CO bond fission in CpFe(CO)$_2$I are also likely to be formed with substantial internal excitation. Some such

fragments formed at the shorter wavelengths investigated in the present study might be expected to have sufficient internal energy to decay further – releasing a secondary CO or I fragment. Energy conservation (Table 1) requires that any such secondary fragments formed via a one (UV) photon dissociation process would be formed with little KE. As Figures 4-6 show, however, none of the images recorded at $\lambda \geq 260$ nm show evidence of I atoms with low kinetic energies, suggesting that the latter possibility (I atom loss via unimolecular decay of internally 'hot' CpFe(CO)I primary products) is at most a minor channel.

4. CONCLUSIONS

This work explores the photoinduced elimination of different ligands from a prototypical transition metal complex in the gas phase. We note the prohibitively high density of excited states that would require consideration in any 'complete' description of the photophysics of such metal complexes, but also highlight the understanding that can be gained simply by considering the electronic structure of the products of the photodissociation.

Photoexcitation of $CpFe(CO)_2I$ is shown to yield translationally excited I atoms and Cp fragments with anisotropic recoil velocity distributions consistent with one-photon induced Fe–I (Fe–Cp) bond fission on one or more dissociative PESs. The recoil velocity distributions imply that the faster fragments (at least) are formed in their respective ground electronic states which, at least in the case of Fe–Cp bond rupture, requires strong spin-orbit mixing at some stage in the excitation/dissociation cycle. This is unsurprising, given the presence of the heavy I atom, and the product energy disposals show parallels with those found following UV photolysis of iodobenzene (and its fluorinated analogues).[38,39] Fe–CO bond fission is not observable with the present experimental set-up, but has been implied in the one previous gas phase UV photolysis study of $CpFe(CO)_2I$ [20] and should be expected given the shallow (*i.e.* at best weakly bonding) nature of many of the calculated excited state PECs along $R_{Fe–CO}$. Though Fe–CO bond breaking on the S_0 PES would be viewed as an archetypal heterolytic bond fission, the corresponding bond cleavage from many of the higher excited states can be understood assuming a 3-electron interaction centred around the Fe–CO bond.

The present gas phase study sheds light on several important factors relating to photoinduced ligand elimination from metal complexes. In the context of $CpFe(CO)_2I$, the observed (and deduced) dissociation products are all neutral species. This finding runs counter to conclusions reached in a previous solution phase study of (visible) light induced Fe–I bond fission in this

molecule, where the observed ligand exchange was rationalized in terms of intermediate ion pair formation.[21] Could solvation (with toluene in that case) afford sufficient stabilization to favor formation of ionized dissociation products? This earlier conclusion could usefully be revisited, in a wider range of solvents, using contemporary transient absorption methods.

More widely, to what extent do the present findings inform our broader understanding of transition metal photochemistry? As Table 1 showed, the lowest energy asymptotes of the fragmentation channels considered here correlate with both singlet and triplet excited states of the parent (in the case of Fe–I bond fission) and with triplet and quintet excited states (in the case of Fe–Cp bond fission). Their involvement highlights the importance of spin-orbit coupling in the present excitation / dissociation processes. The spin-orbit coupling probability will be sensitive to the choice of metal atom and to the constituent ligands and, in the present case, is likely to be much enhanced by the presence of the heavy I atom. Thus it remains unclear to what extent the present conclusions will extrapolate to metal complexes that lack such a heavy atom. In this regard, we note an earlier photolysis study of $CpFe(CO)_2Cl$ in the wavelength range $290 \leq \lambda \leq 370$ nm in a low temperature (12 K) matrix that identified loss of CO but no C–Cl bond fission [40] – an outcome that could be explained by invoking purely singlet state mediated photochemistry. The recent X-ray photoelectron spectroscopy study of the products formed in the $\lambda = 266$ nm photolysis of (gas phase) $Fe(CO)_5$ also concluded that the loss of successive CO ligands occurs solely on singlet PESs,[18] but studies of another Fe(II) complex, iron(II)-tris-bipyridine ($[Fe(bpy)_3]^{2+}$) – in both the gas and solution phase – identify exceptionally efficient spin-orbit mixing as the mechanism for the observed ultrafast excited state decay following MLCT excitation.[1,41-43]

ASSOCIATED CONTENT

Depiction of the 10 orbitals used in the CASSCF calculations. Energies of the ground state parent η^5-$CpFe(CO)_2I$ molecule and various of its possible photofragments, calculated at the DFT/CAM-B3LYP/LANL2DZ level of theory. Fe^+ ion image detected following $\lambda = 275$ nm photolysis and $\lambda = 118.2$ nm photoionization of jet-cooled $CpFe(CO)_2I$ molecules together with the KE_{Fe} distribution derived from the image.

AUTHOR INFORMATION

Corresponding Authors

C.S. Hansen. E-mail: christopher.hansen@unsw.edu.au

B. Marchetti. E-mail: barbara.marchetti@louisiana.edu

T.N.V. Karsili. E-mail: tolga.karsili@louisiana.edu

M.N.R. Ashfold. E-mail: mike.ashfold@bristol.ac.uk

ORCID

C.S. Hansen. 0000-0002-8954-0825

T.N.V. Karsili. 0000-0002-0583-3824

M.N.R. Ashfold. 0000-0001-5762-7048

Notes

The authors declare no competing financial interest.

The raw ion events data and calculation log files can be retrieved from the University of Bristol's research data repository and can be accessed using the following DOI: [link will be added at the post-review stage]

ACKNOWLEDGMENTS

The authors are grateful to the Engineering and Physical Sciences Research Council (EPSRC) for the award of a Programme Grant (EP/L005913) and to Emma Elsdon, Dr. Matthew Bain and Dr. James Smith for their many contributions to the earlier stages of this work. CSH is supported by an Australian Research Council Discovery Early Career Academic Award (DE200100549).

Table 1

Threshold energies for forming selected product combinations defined relative to the singlet ground state of $CpFe(CO)_2I$, calculated at the DFT/CAM-B3LYP/LANL2DZ level of theory. The reported energies are spin-orbit averaged, and not corrected for zero-point energy effects.

Fragmentation Channel	Formation Energy / eV
$^2CpFe(CO)_2 + {}^2I$	1.71
$^4CpFe(CO)_2 + {}^2I$	2.27
$^3CpFe(CO)I + {}^1CO$	1.18
$^1CpFe(CO)I + {}^1CO$	1.87
$^4Fe(CO)_2I + {}^2Cp$	2.29
$^2Fe(CO)_2I + {}^2Cp$	2.71
$^4CpFe(CO) + {}^1CO + {}^2I$	3.08
$^2CpFe(CO) + {}^1CO + {}^2I$	3.89
$^1CpFeI + 2{}^1CO$	3.70
$^4Fe(CO)I + {}^2Cp + {}^1CO$	3.37
$^2Fe(CO)I + {}^2Cp + {}^1CO$	4.23
$^3Fe(CO)_2 + {}^2Cp + {}^2I$	5.81
$^1Fe(CO)_2 + {}^2Cp + {}^2I$	6.63
$^4CpFe + 2{}^1CO + {}^2I$	5.27
$^5Fe(CO) + {}^2Cp + {}^1CO + {}^2I$	7.06
$^3Fe(CO) + {}^2Cp + {}^1CO + {}^2I$	7.13

Figure Captions

Figure 1

Electronic absorption spectrum of $CpFe(CO)_2I$ in cyclohexane solution along with a schematic of the parent molecular structure and a bracket indicating the range of photolysis wavelengths used in this study.

Figure 2

Molecular orbital (MO) energy level diagram of $CpFe(CO)_2I$. The *d* orbitals of the Fe atom are shown on the left, the orbitals of the respective ligands are shown on the right and the resulting parent MOs appear in the central column.

Figure 3

Ion mass spectrum obtained by λ = 118.2 nm photoionization following λ = 275 nm excitation of a jet-cooled sample of $CpFe(CO)_2I$ seeded in helium, along with the corresponding one color spectra obtained with one or other laser beam blocked. The higher *m*/*z* signals are displayed using progressively greater vertical expansions.

Figure 4

Representative images of (a) I_{tot} and (d) Cp fragments (detected by SPI) and of (b) I and (c) I* fragments (REMPI detection) resulting from photolysis of $CpFe(CO)_2I$ with linearly polarized light of λ ~266 nm (the electric vector, $\boldsymbol{\varepsilon}$, is aligned vertically as shown by the double headed arrow in panel (a)). The SPI-detected ion images, (a) and (d), were recorded at a pump wavelength λ = 266.55 nm, while the REMPI detected ions corresponding to I and I*, (b) and (c), were recorded at λ = 266.49 and λ = 266.65 nm, respectively. The right-hand panels show the fragment recoil velocity distributions (individually normalized to the same peak intensity) overlayed with the *v*-dependent best-fit β anisotropy parameters (red circles) derived from each image. The β parameters are only displayed in the range between v >100 m s^{-1} and where the high *v* tail in the velocity distribution had decreased to 10% of its peak intensity.

Figure 5

(a) KE distributions of the I_{tot} fragments detected by SPI at ten photolysis wavelengths (listed in the legend, units are nm), each normalized to the same peak intensity. (b) Plot of $KE_{I(mp)}$ *vs* E_{phot} determined therefrom where the error bars represent the 95% confidence limits.

Figure 6

KE distributions of the I and I* products detected by REMPI at (a) λ ~304.5 nm, (b) λ ~277.6 nm and (c) λ ~266.5 nm, plotted together with those for the λ = 118.2 nm SPI detected I_{tot} fragments obtained at the nearest photolysis wavelength. The various distributions in each plot have each been normalized to the same peak intensity.

Figure 7

(a) KE distributions of Cp fragments detected by SPI at ten different photolysis wavelengths (listed in the legend, units are nm), with (b) a plot of $KE_{Cp(mp)}$ *vs* E_{phot} where the error bars represent the 95% confidence limits.

Figure 8

Unrelaxed adiabatic SOA CASSCF PECs for $CpFe(CO)_2I$ along R_{Fe-I} for the S_0 state (filled black circles) and the first few (a) singlet and (b) triplet excited states, calculated by scanning from large R_{Fe-I} while maintaining the rest of the nuclear framework at the S_0 state minimum energy geometry. The vertical bar shown at the far right of just the lowest asymptote in both plots illustrates the magnitude of the I/I* spin-orbit splitting.

Figure 9

Unrelaxed adiabatic SOA CASSCF PECs for $CpFe(CO)_2I$ along R_{Fe-CO} for the S_0 state (filled black circles) and the first few (a) singlet and (b) triplet excited states, calculated by scanning from large R_{Fe-CO} while maintaining the rest of the nuclear framework at the S_0 state minimum energy geometry.

Figure 1

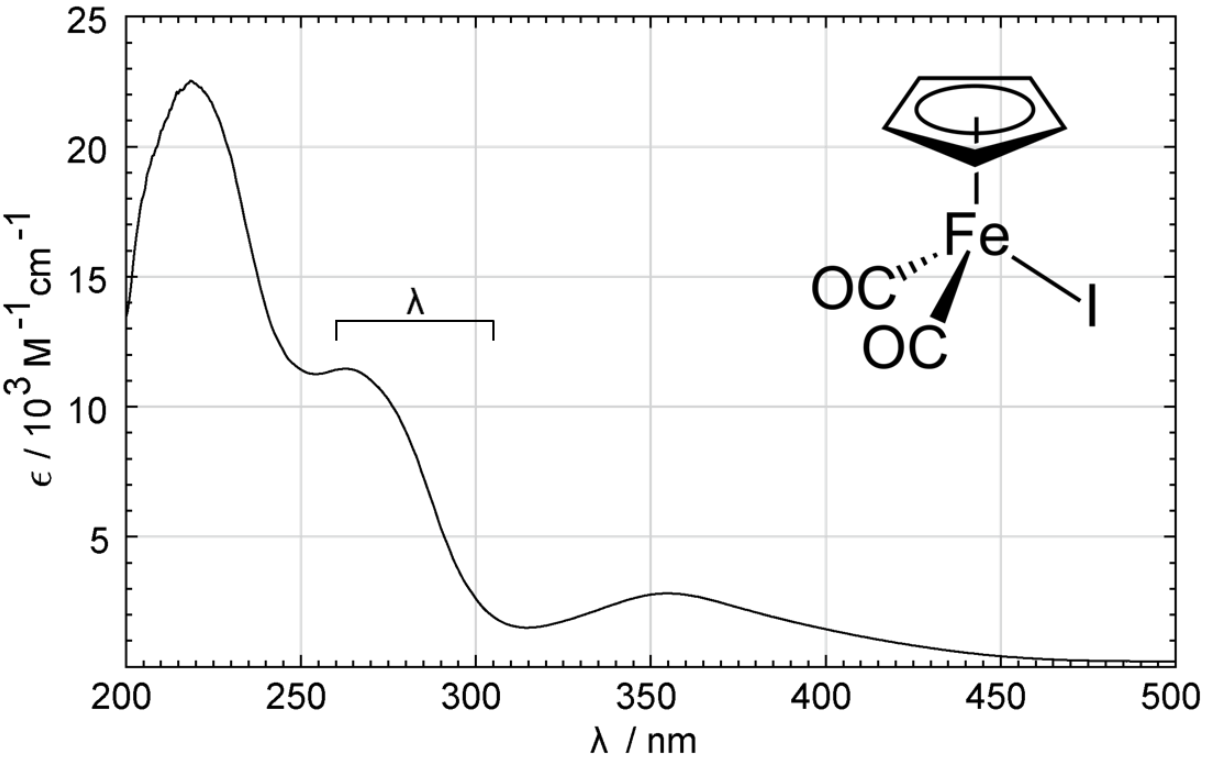
25
20
15
10
5
ϵ / 10^3 M^-1 cm^-1
λ
200
250
300
350
400
450
500
λ / nm
Fe
OC
OC
I

Figure 2

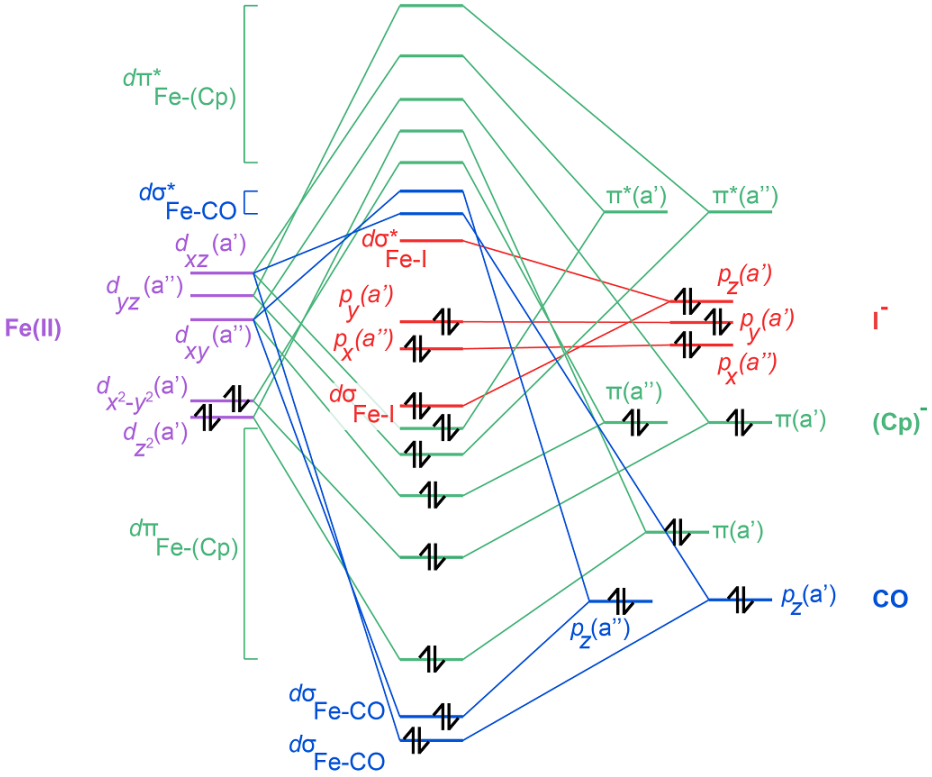
dπ* Fe-(Cp)
dσ* Fe-CO
d xz (a')
d yz (a'')
d xy (a'')
d x²-y² (a')
d z² (a')
Fe(II)
dπ Fe-(Cp)
dσ Fe-CO
dσ Fe-CO
dσ* Fe-I
p y (a')
p x (a'')
dσ Fe-I
π*(a')
π*(a'')
π(a'')
π(a')
π(a')
p z (a'')
p z (a')
p z (a')
p y (a')
p x (a'')
I⁻
(Cp)⁻
CO

Figure 3

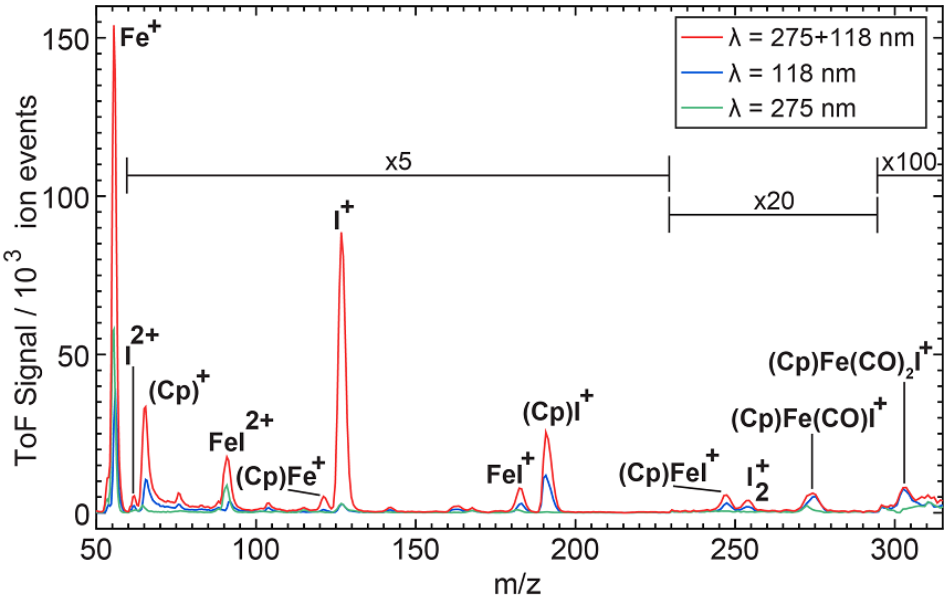
λ = 275+118 nm
λ = 118 nm
λ = 275 nm
x5
x20
x100
Fe+
I2+
(Cp)+
FeI2+
(Cp)Fe+
I+
FeI+
(Cp)I+
(Cp)FeI+
I2+
(Cp)Fe(CO)I+
(Cp)Fe(CO)2I+
ToF Signal / 10^3 ion events
m/z
0
50
100
150
200
250
300

Figure 4

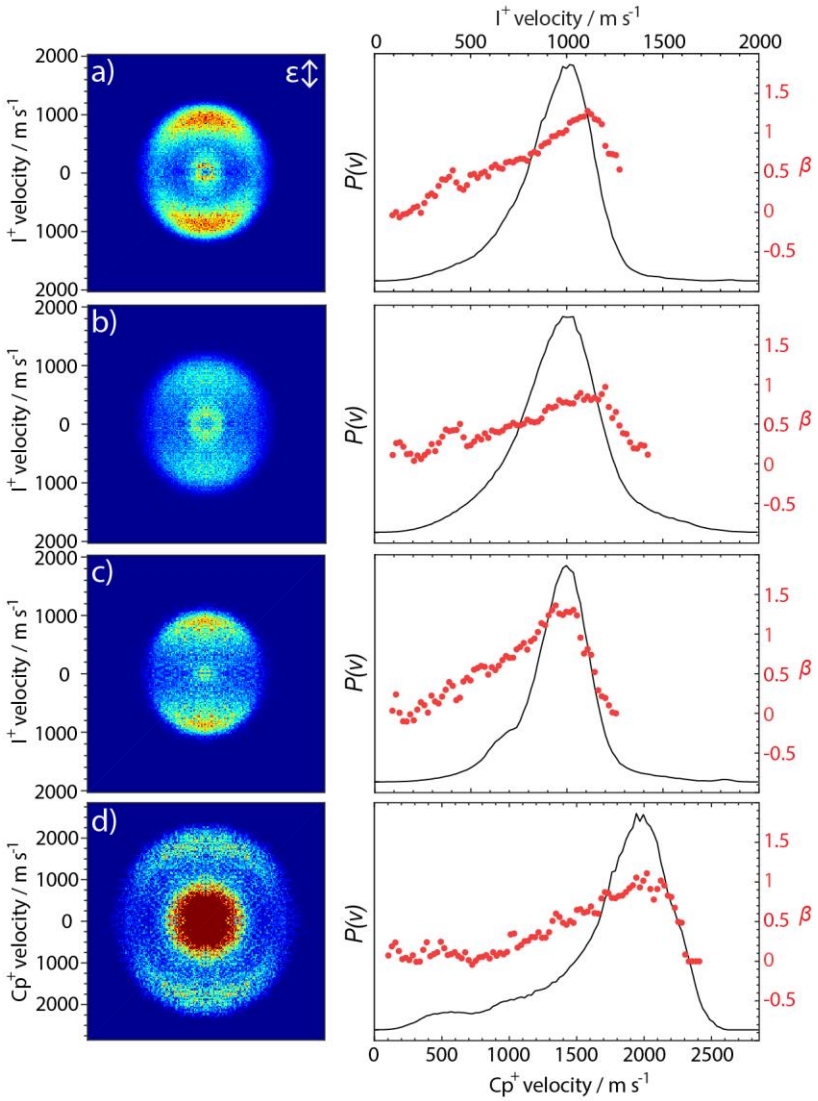
a)
b)
c)
d)
ε↕
I+ velocity / m s-1
Cp+ velocity / m s-1
P(v)
β
2000
1000
0
1000
2000
0
500
1000
1500
2000
2500
1.5
1
0.5
0
-0.5

Figure 5

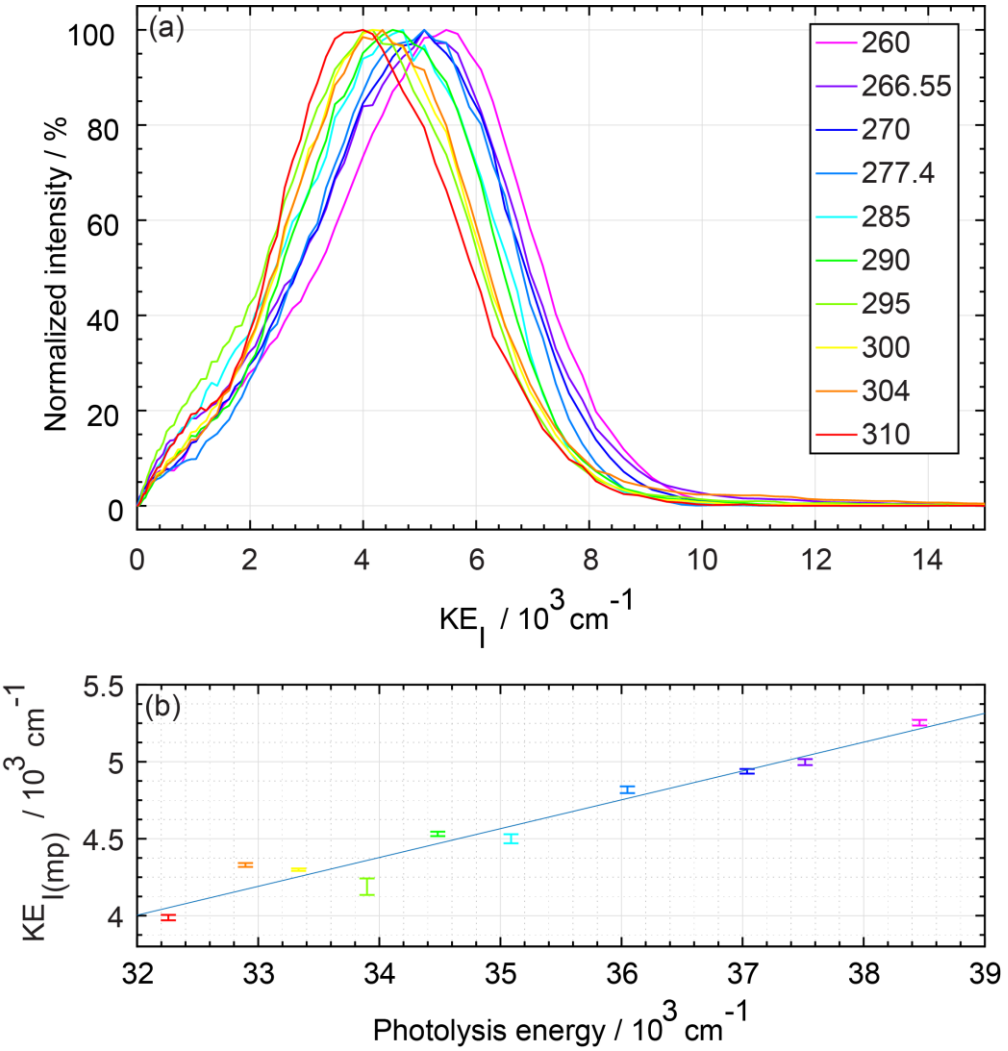
(a)
Normalized intensity / %
100
80
60
40
20
0
0
2
4
6
8
10
12
14
KE_I / 10^3 cm^-1
260
266.55
270
277.4
285
290
295
300
304
310
(b)
KE_I(mp) / 10^3 cm^-1
5.5
5
4.5
4
32
33
34
35
36
37
38
39
Photolysis energy / 10^3 cm^-1

Figure 6

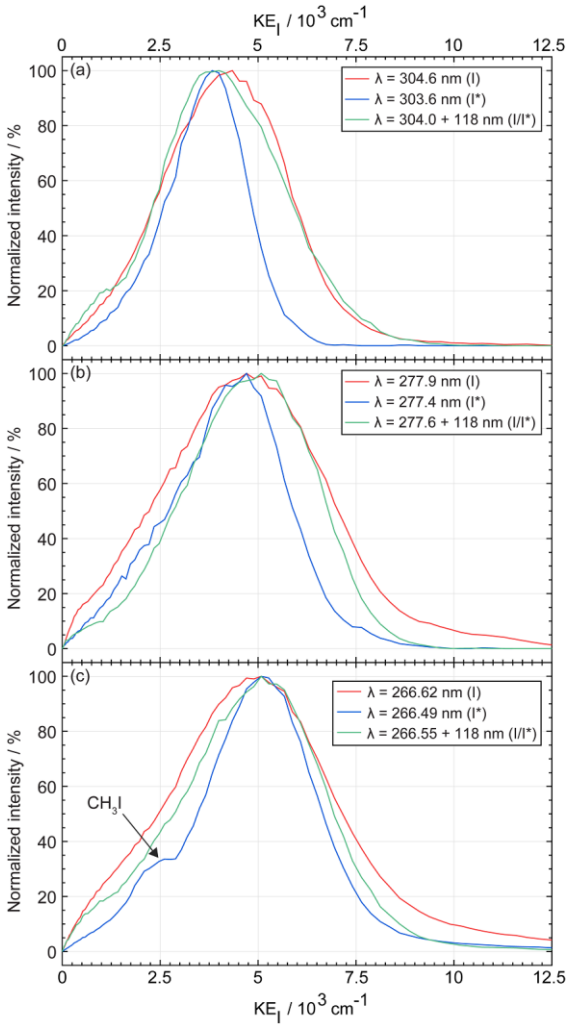
KE$_I$ / 10^3 cm^{-1}
0
2.5
5
7.5
10
12.5
(a)
λ = 304.6 nm (I)
λ = 303.6 nm (I*)
λ = 304.0 + 118 nm (I/I*)
(b)
λ = 277.9 nm (I)
λ = 277.4 nm (I*)
λ = 277.6 + 118 nm (I/I*)
(c)
λ = 266.62 nm (I)
λ = 266.49 nm (I*)
λ = 266.55 + 118 nm (I/I*)
CH$_3$I
Normalized intensity / %
0
20
40
60
80
100

Figure 7

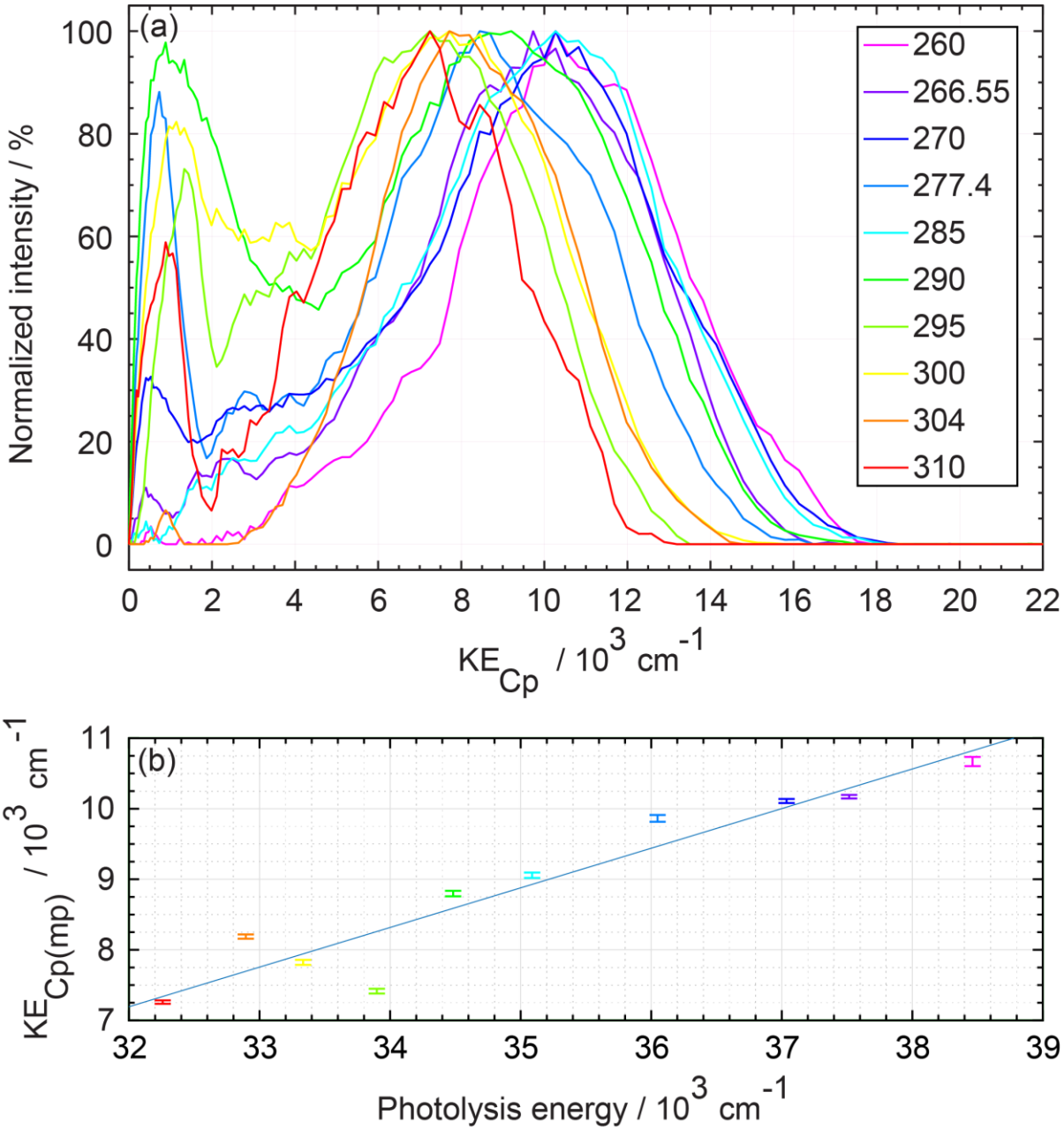
(a)
Normalized intensity / %
100
80
60
40
20
0
0
2
4
6
8
10
12
14
16
18
20
22
KE$_{Cp}$ / 10^{3} cm^{-1}
260
266.55
270
277.4
285
290
295
300
304
310
(b)
KE$_{Cp(mp)}$ / 10^{3} cm^{-1}
11
10
9
8
7
32
33
34
35
36
37
38
39
Photolysis energy / 10^{3} cm^{-1}

Figure 8

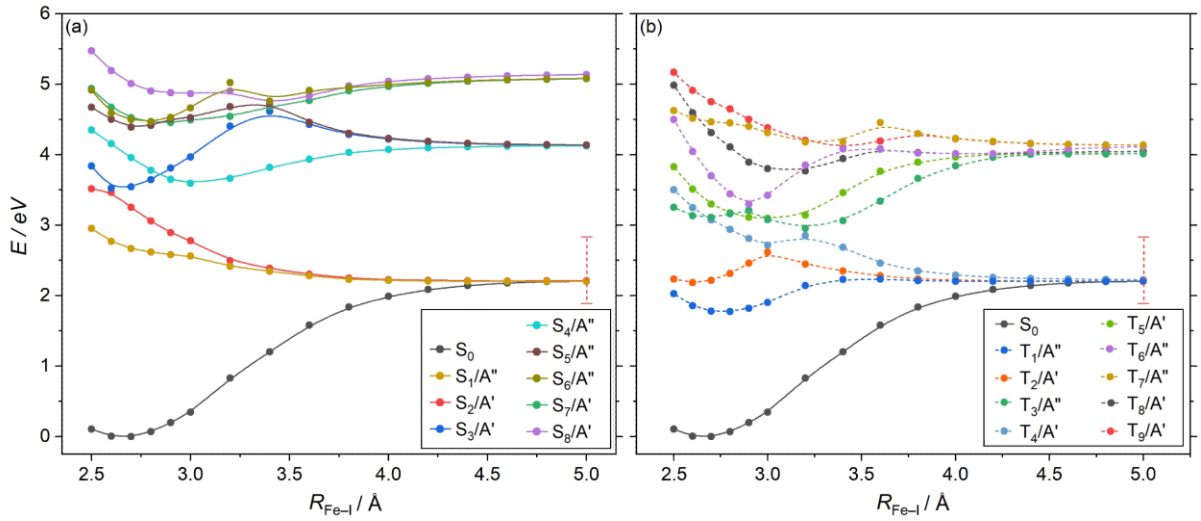
(a)
(b)
E / eV
R_Fe–I / Å
S0
S1/A"
S2/A'
S3/A'
S4/A"
S5/A"
S6/A"
S7/A'
S8/A'
T1/A"
T2/A'
T3/A"
T4/A'
T5/A'
T6/A"
T7/A"
T8/A'
T9/A'

Figure 9

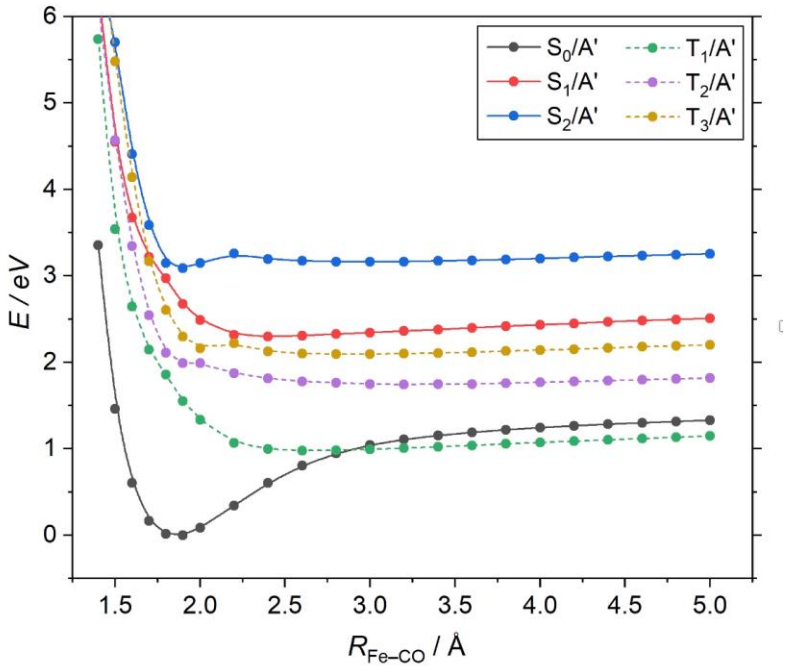
S0/A'
S1/A'
S2/A'
T1/A'
T2/A'
T3/A'
E / eV
RFe–CO / Å
0
1
2
3
4
5
6
1.5
2.0
2.5
3.0
3.5
4.0
4.5
5.0

TOC graphic

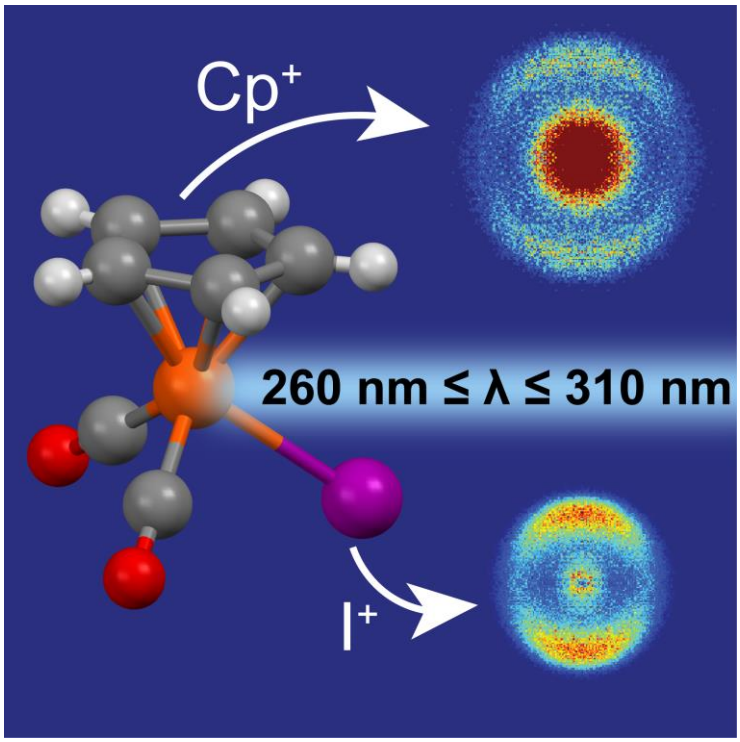

REFERENCES

[1] T.J. Penfold, E. Gindensperger, C. Daniel, C. M. Marian, Chem. Rev. **118**, 6975 (2018) and references therein.

[2] S. Mathew, A. Yella, P. Gao, R. Humphry-Baker, B.F.E. Curchod, N. Ashari-Astani, I. Tavernelli, U. Rothlisberger, M.K. Nazeeruddin, M. Grätzel, Nat. Chem. **6**, 242 (2014).

[3] P. Agostinis, K. Berg, K.A. Cengel, T.H. Foster, A.W. Girotti, S.O. Gollnick, S.M. Hahn, M.R. Hamblin, A. Juzeniene, D. Kessel, M. Korbelik, J. Moan, P. Mroz, D. Nowis, J. Piette, B.C. Wilson, J. Golab, CA-A Cancer J. Clin. **61**, 250 (2011).

[4] H. Abrahamse, M.R. Hamblin, Biochem. J. **473**, 347 (2016).

[5] M. Brookhart, M.L.H. Green, G. Parkin, Proc. Natl. Acad. Sci. **104**, 6908 (2007).

[6] H.M. Yau, A.I. McKay, H. Hesse, R. Xu, M. He, C.E. Holt, G.E. Ball, J. Amer. Chem. Soc. **138**, 281 (2016).

[7] M.I. Litter, Appl. Catal. B – Environmental **23**, 89 (1999).

[8] M.N. Hopkinson, B. Sahoo, J.L. Li, F. Glorius, Chemistry – A European J. **20**, 3874 (2014).

[9] R.N. Perutz, O. Torres, A. Vlćek, Photochemistry of Metal Carbonyls, in Comprehensive Inorganic Chemistry II, (eds. J. Reedijk, K.Poeppelmeier), Elsevier, 229-253 (2013).

[10] I.P. Clark, M.W. George, G.M. Greetham, E.C. Harvey, C. Long, J.C. Manton, M.T. Pryce, J. Phys Chem. A **114**, 11425 (2010).

[11] S. Bellemin-Laponnaz, S. Dagorne, Chem. Rev. **114**, 8747 (2014).

[12] A. Freedman, R. Bersohn, J. Amer. Chem. Soc. **100**, 4116 (1978).

[13] D.G. Leopold, V. Vaida, J. Amer. Chem. Soc. **106**, 3720 (1984).

[14] Z. Karny, R. Naaman, R.N. Zare, Chem. Phys. Lett. **59**, 33 (1978).

[15] T.A. Seder, A.J. Ouderlirk, E. Weitz, J. Chem. Phys. **85**, 1977 (1986).

[16] L. Bañares, T. Baumert, M. Bergt, B. Kiefer, G. Gerber, J. Chem. Phys. **108**, 5799 (1998).

[17] S.A. Trushin, W. Fuss, K.L. Kompa, W.E. Schmid, J. Phys. Chem. A. **104**, 1997 (2000).

[18] Ph.Wernet, T. Leitner, I. Josefsson, T. Mazza, P.S. Miedema, H. Schröder, M. Beye, K. Kunnus, S. Schreck, P. Radcliffe, S. Düsterer, M. Meyer, M. Odelius, A. Föhlisch, J. Chem. Phys. **146**, 211103 (2017).

[19] T. Malcomson, R.G. McKinlay, M.J. Paterson, ChemPhotoChem **3**, 1 (2019).

[20] M. Bergt, T. Brixner, C. Dietl, B. Kiefer, G. Gerber, J. Organometal. Chem. **661**, 199 (2002).

[21] C.E. Borja, V. Jakábek, A.J. Lees, Inorg. Chem. **37**, 2281 (1998).

[22] R.A. Ingle, C.S. Hansen, E. Elsdon, M. Bain, S.J. King, J.W.L. Lee, M. Brouard, C. Vallance, R. Turchetta, M.N.R. Ashfold, J. Chem. Phys **147**, 013914 (2017).

[23] M. Bain, C.S. Hansen, M.N.R. Ashfold, J. Chem. Phys. **149**, 081103 (2018).

[24] J.J. John, M. Brouard, A. Clark, J. Crooks, E. Halford, L. Hill, J.W.L. Lee, A. Nomerotski, R. Pisarczyk, I. Sedgwick, C. S. Slater, R. Turchetta, C. Vallance, E. Wilman, B. Winter, W.H. Yuen, J. Instrum., **7**, C08001 (2012).

[25] T. Yanai, D.P. Tew, N.C. Handy, Chem. Phys. Lett. **393**, 51 (2004).

[26] M.J Frisch, G.W. Trucks, H.B. Schlegel, G.E. Scuseria *et al*., Gaussian 09, Revision D.01, Gaussian, Inc. (2013).

[27] P.J. Hay, W.R. Wadt, J. Chem. Phys. **82**, 270 (1985).

[28] H.J. Werner, P.J. Knowles, G. Knizia, F.R. Manby *et al*., MOLPRO, version 2015.1 (2015).

[29] T.N.V. Karsili, B. Marchetti, M.N.R. Ashfold, Chem. Phys. **515**, 464 (2018).

[30] R.N. Zare, Mol. Photochem. **4**, 1 (1972).

[31] H. Fan, S.T. Pratt, J. Phys. Chem. A **111**, 3901 (2007).

[32] Y.R. Luo, Comprehensive Handbook of Chemical Bond Energies, CRC Press, Boca Raton, FL, 2007.

[33] P.J. Linstrom, W.G. Mallard, NIST Chemistry WebBook, *NIST Standard Reference Database Number 69*, National Institute of Standards and Technology, Gaithersburg MD, 20899, doi:10.18434/T4D303.

[34] D.L. Lichtenberger, R.F. Fenske, J. Amer. Chem. Soc. **96**, 50 (1976).

[35] P.B. Armentrout, J. Simons, J. Amer. Chem. Soc. **114**, 8627 (1992).

[36] Y. Amatatsu, K. Morokuma, S. Yabushita, J. Chem. Phys. **104**, 9783 (1996).

[37] A.T.J.B. Eppink, D.H. Parker, J. Chem. Phys. **110**, 832 (1999).

[38] A.G. Sage, T.A.A. Oliver, D. Murdock, M.B. Crow, G.A.D. Ritchie, J.N. Harvey, M.N.R. Ashfold, Phys. Chem. Chem. Phys. **13**, 8075 (2011).

[39] D. Murdock, M.B. Crow, G.A.D. Ritchie, M.N.R. Ashfold, J. Chem. Phys **136**, 124313 (2012).

[40] R.H. Hooker, K.A. Mahmoud, A.J. Rest, J. Chem. Soc. Dalton Trans., 1231 (1990).

[41] G. Auböck, M. Chergui, *Nat. Chem.* **7**, 629 (2015).

[42] M. Papai, G. Vanko, T. Rozgonyi, T.J. Penfold, J. Phys. Chem. Lett. **7**, 2009 (2016).

[43] K.S. Kjaer, T.B. Van Driel, T.C.B. Harlang, K. Kunnus, *et al*., Chem. Sci. **10**, 5749 (2019).